

# Single-Ion Conducting Soft Electrolytes for Semi-Solid Lithium Metal Batteries Enabling Cell Fabrication and Operation under Ambient Conditions

Kyeong-Seok Oh, Jung-Hui Kim, Se-Hee Kim, Dongrak Oh, Sun-Phil Han, Kwangeun Jung, Zhuoyi Wang, Liyi Shi, Yongxiang Su, Taeun Yim,\* Shuai Yuan,\* and Sang-Young Lee\*

Despite their potential as post lithium-ion batteries, solid-state Li-metal batteries are struggling with insufficient electrochemical sustainability and ambient operation limitations. These challenges mainly stem from lack of reliable solid-state electrolytes. Here, a new class of single-ion conducting quasi-solid-state soft electrolyte (SICSE) for practical semi-solid Li-metal batteries (SSLMBs) is demonstrated. The SICSE consists of an ion-rectifying compliant skeleton and a nonflammable coordinated electrolyte. Rheology-tuned SICSE pastes, in combination with UV curing-assisted multistage printing, allow fabrication of seamlessly integrated SSLMBs (composed of a Li metal anode and  $\text{LiNi}_{0.8}\text{Co}_{0.1}\text{Mn}_{0.1}$  cathode) without undergoing high-pressure/high-temperature manufacturing steps. The single-ion conducting capability of the SICSE plays a viable role in stabilizing the interfaces with the electrodes. The resulting SSLMB full cell exhibits stable cycling performance and bipolar configurations with tunable voltages and high gravimetric/volumetric energy densities ( $476 \text{ Wh kg}_{\text{cell}}^{-1}/1102 \text{ Wh L}_{\text{cell}}^{-1}$  at four-stacked cells with  $16.656 \text{ V}$ ) under ambient operating conditions, along with low-temperature performance, mechanical foldability, and nonflammability.

energy densities and safety.<sup>[2,3]</sup> A key enabling technology for the solid-state LMBs undoubtedly lies with reliable solid-state  $\text{Li}^+$  conductors.<sup>[4,5]</sup>

Previous studies on solid-state  $\text{Li}^+$  conductors have mostly focused on inorganic solid electrolytes such as sulfides and oxides. Despite their solid-state feature and ideal  $\text{Li}^+$  transference number ( $t_{\text{Li}^+} = 1$ ), the inorganic solid electrolytes have suffered from interfacial/grain-boundary resistances, thickness issues, mechanical rigidity, and dendrite growth through interstitial voids.<sup>[6,7]</sup> Recently, argyrodite-type sulfides ( $\text{Li}_6\text{PS}_5\text{Cl}$ ) combined with silver-carbon composite anodes enabled the fabrication of high-energy long-cycling solid-state LMBs.<sup>[8]</sup> However, the sophisticated isostatic pressing technique and high-temperature ( $60^\circ\text{C}$ ) operating conditions were needed to electrochemically activate the cells. Besides, the aforementioned inorganic solid electrolytes, solid-polymer


electrolytes have been investigated owing to their ease of processability, mechanical flexibility, and close interfacial contact with electrodes.<sup>[9,10]</sup> However, the solid polymer electrolytes have shown limitations in ionic conductivity, operating temperature, electrochemical stability window, and complicated synthesis.<sup>[11,12]</sup> Additionally, many solid polymer electrolytes tend to contain freely movable anions which trigger concentration polarization, unwanted side reactions with electrodes, and growth of Li dendrites,<sup>[13,14]</sup> hindering their practical uses in solid-state LMBs.

## 1. Introduction

The forthcoming smart energy era, including the widespread popularity of flexible/wearable electronics, electric vehicles (EVs), and grid-scale energy storage, has spurred the relentless pursuit of high-energy-density batteries with electrochemical longevity.<sup>[1]</sup> Solid-state lithium (Li)-metal batteries (LMBs) have recently garnered considerable attention as a promising candidate for post Li-ion batteries owing to their exceptional

K.-S. Oh, S.-Y. Lee  
Department of Chemical and Biomolecular Engineering  
Yonsei University  
50 Yonsei-ro, Seodaemun-gu, Seoul 120-749, Republic of Korea  
E-mail: syleek@yonsei.ac.kr  
J.-H. Kim, S.-H. Kim, D. Oh  
Department of Energy Engineering  
School of Energy and Chemical Engineering  
Ulsan National Institute of Science and Technology (UNIST)  
Ulsan 44919, Korea

S.-P. Han  
UNIST Central Research Facilities  
Ulsan National Institute of Science and Technology (UNIST)  
Ulsan 44919, Republic of Korea  
K. Jung, T. Yim  
Department of Chemistry  
Incheon National University  
119 Academy-ro, Yeonsu-Gu, Incheon 406-772, Republic of Korea  
E-mail: yte0102@inu.ac.kr  
Z. Wang, L. Shi, Y. Su, S. Yuan  
Research Centre of Nanoscience and Nanotechnology  
Shanghai University  
99 ShangDa Road, Shanghai 200444, China  
E-mail: s.yuan@shu.edu.cn

 The ORCID identification number(s) for the author(s) of this article can be found under <https://doi.org/10.1002/aenm.202101813>.

DOI: 10.1002/aenm.202101813

In addition to enhancing the bulk properties of solid-state electrolytes mentioned above, much attention should be paid to cell design and electrochemical compatibility of solid-state electrolytes with electrodes.<sup>[15,16]</sup> More notably, to enable practically viable solid-state LMBs as a post Li-ion battery in terms of electrochemical performance and mass production, it is highly preferable that solid-state LMBs should be fabricated and also operated under ambient conditions without relying on precisely defined pressing and high temperatures.<sup>[17,18]</sup>

Here, we present a single-ion conducting quasi-solid-state soft electrolyte (denoted as “SICSE”) as a new material strategy for practical semi-solid LMBs (SSLMBs) that allow cell fabrication and operation under ambient conditions. The SICSE is composed of an ion-rectifying compliant skeleton and a non-flammable coordinated electrolyte. The ion-rectifying compliant skeleton consists of a ultraviolet (UV)-cured cationic copolymer (ethoxylated trimethylolpropane triacrylate (ETPTA)/diallyl dimethyl ammonium-bis(trifluoromethane sulfonyl) imide (DADMA-TFSI)) and titanium/silica-modified alumina nanoparticles ( $\text{Ti-SiO}_2\text{@Al}_2\text{O}_3$ ), in which the ETPTA and DADMA-TFSI can provide structural integrity and ion-rectifying (i.e., anion-trapping) effect, respectively, and the  $\text{Ti-SiO}_2\text{@Al}_2\text{O}_3$  nanoparticles serve as a rheology-tuning and anion-trapping (through Lewis acid-base interactions) agent. The coordinated electrolyte is 4 M lithium bis(fluorosulfonyl)imide (LiFSI) in propylene carbonate (PC)/fluoroethylene carbonate (FEC), which shows electrochemical stability with Li metal anodes and high-voltage cathodes due to the well-coordinated ion-solvent complexes along with thermal stability (boiling point: PC = 242 °C and FEC = 212 °C)<sup>[19]</sup> and nonflammability. The resulting SICSE exhibits high ionic conductivity,  $\text{Li}^+$  transference number close to unity ( $t_{\text{Li}^+} = 0.91$ ), wide electrochemical stability window, mechanical flexibility, and nonflammability.

To develop high-energy-density SSLMBs, a thin Li metal anode is coupled with a high-capacity/high-voltage  $\text{LiNi}_{0.8}\text{Co}_{0.1}\text{Mn}_{0.1}\text{O}_2$  (NCM811) cathode in the presence of SICSE. Rheology-tuned SICSE pastes are subjected to a UV-curing-assisted stepwise printing process, thereby enabling facile fabrication of seamlessly integrated SSLMBs without undergoing high-pressure/high-temperature sintering steps that are typically required for inorganic solid electrolytes-based solid-state LMBs. The soft feature of the SICSE alleviates the concerns of grain-boundary resistance and the interfacial instability of electrolyte-electrodes which have posed longstanding challenges in inorganic solid electrolytes. In addition, the single-ion conducting capability of the SICSE contributes to stabilizing the interfaces with Li metal anodes and NCM811 cathodes.

Driven by the chemical/structural uniqueness of the SICSE and monolithic full cell architecture described above, the SSLMB (composed of Li metal anode and NCM811 cathode) full cell exhibits reliable electrochemical performance, cycling retention, rate capability, and bipolar configurations with tunable voltages and high gravimetric/volumetric energy densities (476 Wh  $\text{kg}_{\text{cell}}^{-1}$ /1102 Wh  $\text{L}_{\text{cell}}^{-1}$  at four-stacked cells with 16.656 V) under ambient operating conditions. Moreover, the low-temperature performance, foldability, and safety far exceed those attainable with inorganic electrolyte-based solid-state LMBs.

## 2. Results and Discussion

### 2.1. Fabrication of the SICSEs at Ambient Conditions

The fabrication procedure of the SICSE along with its chemical structure is schematically depicted in **Figure 1a**. An optimal composition ratio (coordinated electrolyte (4 M LiFSI in PC/FEC = 93/7 (v/v))/compliant skeleton precursor) of the SICSE paste was set to 42.5/57.5 (w/w), in which a further increase of coordinated electrolyte content failed to obtain a self-standing film (**Figure S1a**, Supporting Information). In the compliant skeleton precursor, the ratio of UV-curable monomer mixture (ETPTA/DADMA-TFSI)/ $\text{Ti-SiO}_2\text{@Al}_2\text{O}_3$  nanoparticles was set to 50/50 (w/w) by exploring the rheological requirements for the printing process (**Figure S1b**, Supporting Information). In the UV-polymerizable monomer mixture, the ratio of ETPTA/DADMA-TFSI was set to 40/60 (w/w) by considering the  $\text{Li}^+$  conductivity,  $\text{Li}^+$  transference number ( $t_{\text{Li}^+}$ ), and self-standing film formation of the UV-cured cationic copolymers after swelling with the coordinated electrolyte (**Figure S1c**, Supporting Information).

The above-prepared SICSE paste was stencil-printed directly on a Li metal foil without using any processing solvents and then solidified after exposure to UV irradiation. The obtained SICSE showed characteristic Fourier transform infrared (FTIR) peaks of the ETPTA ( $\nu_{\text{C}=\text{O}}$ ,  $\nu_{\text{C}-\text{H}}$ ) and DADMA-TFSI ( $\nu_{\text{C}-\text{N}}$  and  $\nu_{\text{C}-\text{F}}$ ) (**Figure S2**, Supporting Information). The UV irradiation-driven curing process was verified by monitoring the change in the FTIR spectroscopy peaks assigned to the acrylic  $\text{C}=\text{C}$  bonds<sup>[20,21]</sup> of the UV-curable monomer (**Figure S3**, Supporting Information). In addition, the  $^1\text{H}$  nuclear magnetic resonance (NMR) analysis (**Figure S4a**, Supporting Information) exhibited the characteristic peaks assigned to  $\text{N}-\text{CH}_3$  (3.54 ppm) and  $\text{N}-\text{CH}_2$  (4.01 ppm), verifying the successful copolymerization of the ETPTA and the DADMA-TFSI. The molecular weight information of the cationic copolymer (ETPTA-(DADMA-TFSI)) was obtained using gel permeation chromatography (GPC) measurement:  $M_w$  (weight-average molecular weight) = 309 262 g  $\text{mol}^{-1}$  (**Figure S4b**, Supporting Information). **Figure 1b** shows that the printed SICSE was monolithically integrated with the Li metal foil, which was verified by analyzing electrochemical impedance spectroscopy (EIS) spectra. The printed SICSE-Li metal assembly showed lower cell impedance compared to the simple stacking of a self-standing SICSE on a Li metal foil (**Figure S5**, Supporting Information), exhibiting an intimate interfacial contact between the printed SICSE and Li metal foil. In addition, the surface and cross-sectional energy-dispersive X-ray spectroscopy (EDS) mapping images showed a homogeneous distribution of elements in the SICSE, which originated from the DADMA-TFSI (for C and N) and  $\text{Ti-SiO}_2\text{@Al}_2\text{O}_3$ , (for Al, Si, and Ti), respectively (**Figures S6 and S7**, Supporting Information). It is also noteworthy that the absence of processing solvents removed the time- and cost-consuming drying steps and prevented processing solvent-triggered unwanted side reactions typically seen with Li metals. The SICSE paste (i.e., prior to the UV curing) showed typical shear-thinning rheological behavior (**Figure S8a**, Supporting Information). The viscoelasticity analysis of the SICSE paste exhibited the higher storage modulus ( $G'$ ) than the

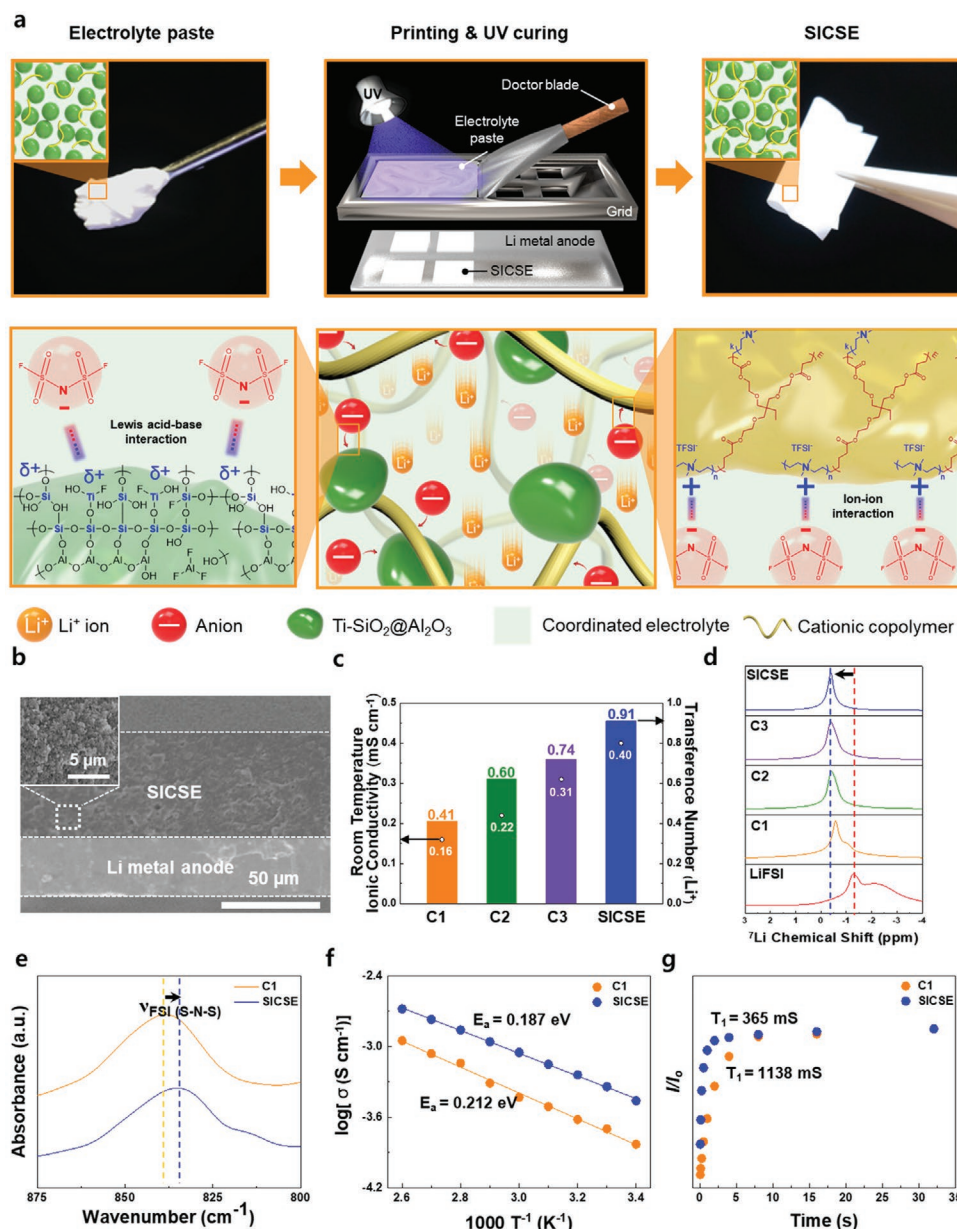


**Figure 1.** Fabrication of the SICSE at ambient conditions and its single-ion conducting characteristics. a) Schematic representation depicting the fabrication procedure of the SICSE (upper image) and its components bearing anion-trapping capability (bottom image). b) Cross-sectional SEM image of the printed SICSE on a Li metal anode. c) Room-temperature ionic conductivity ( $\sigma$ ) and Li<sup>+</sup> transference number ( $t_{\text{Li}^+}$ ) of the SICSE and control samples (C1, C2, and C3). d) <sup>7</sup>Li NMR spectra of the SICSE, control samples (C1, C2, and C3), and LiFSI. e) FTIR spectra of the SICSE and C1. f) Arrhenius plot for the ionic conductivity of SICSE and C1. g) Inversion–recovery plots obtained from <sup>7</sup>Li MAS NMR spectra.

loss modulus ( $G''$ ) in the low shear stress region and the cross-over of  $G'$  and  $G''$  in the high shear stress region, indicating a thixotropic fluid behavior<sup>[20,21]</sup> that is suitable for the stencil printing process (Figure S8b, Supporting Information). Intriguingly, this well-tuned rheological property enabled the fabrication of a letter-shaped SICSE (inset of Figure S8b, Supporting Information).

The single Li<sup>+</sup> conduction characteristics of the SICSE were investigated using a potentiostatic polarization method,<sup>[22]</sup> in which a self-standing SICSE film and three control samples (denoted as C1, C2, and C3, Figure S9, Supporting Information)

were fabricated using the aforementioned UV-curing-assisted printing method. The SICSE showed the highest room-temperature ionic conductivity ( $\sigma = 0.4 \text{ mS cm}^{-1}$ ) and Li<sup>+</sup> transference number ( $t_{\text{Li}^+} = 0.91$ ) compared to the control samples (Figure 1c, Figure S10 and Table S1, Supporting Information). Notably, the high  $t_{\text{Li}^+}$  value demonstrated the anion-trapping effect enabled by the ion-rectifying compliant skeleton (i.e., the coupled effect of DADMA and Ti-SiO<sub>2</sub>@Al<sub>2</sub>O<sub>3</sub> nanoparticles), which is conceptually illustrated in Figure 1a. The positively charged ammonium groups of the DADMA in the cationic copolymer are known to trap anions in the electrolytes owing



to their ion-rectifying effect<sup>[23–25]</sup> that enables selective cation transport. Meanwhile, the Ti-SiO<sub>2</sub>@Al<sub>2</sub>O<sub>3</sub> nanoparticles were prepared by depositing Ti-doped SiO<sub>2</sub> on the surface of Al<sub>2</sub>O<sub>3</sub> (Figure S11, Supporting Information). In the Ti-doped SiO<sub>2</sub>, Ti doping<sup>[26,27]</sup> was conducted to increase the amount of Lewis acid sites in the SiO<sub>2</sub>. As a result, the synthesized Ti-SiO<sub>2</sub>@Al<sub>2</sub>O<sub>3</sub> nanoparticles possessed Lewis acid sites which can bind anions via the Lewis acid–base interactions.<sup>[28]</sup> This was verified by observing the high zeta potential and the characteristic peaks assigned to the Lewis acid site (1656 cm<sup>−1</sup>) in the in situ FTIR spectra (Figure S12, Supporting Information).

This high  $t_{\text{Li}^+}$  value of the SICSE was further investigated by conducting a <sup>7</sup>Li magic-angle spinning (MAS) NMR and FTIR analysis. In comparison to the control samples (including the bare LiFSI salt), the SICSE showed a narrower width in the <sup>7</sup>Li spectrum and a downfield shift (Figure 1d), revealing the prevalence of freely mobile Li<sup>+</sup> ions.<sup>[29,30]</sup> This result was confirmed by a downfield shift of the characteristic vibration peak of the FSI<sup>−</sup> ions (Figure 1e), demonstrating the vital role of the ion-rectifying compliant skeleton (UV-cured cationic copolymer/Ti-SiO<sub>2</sub>@Al<sub>2</sub>O<sub>3</sub>) in the anion-trapping mechanism.

The ionic conductivity of the SICSE was estimated as a function of temperature (varying from room temperature to 100 °C). The SICSE showed higher ionic conductivity over a wide range of temperatures and smaller activation energy ( $E_a$ , obtained from Arrhenius equation) as compared to those of the C1 (a control sample) despite the restricted migration of anions, exhibiting that the Li<sup>+</sup> transport could be accelerated in the SICSE (Figure 1f, Figure S13 and Table S2, Supporting Information). To verify this unusual ion conduction behavior, we performed an inversion-recovery experiment at room temperature using <sup>7</sup>Li NMR spectroscopy. From the normalized intensities ( $I/I_0$ ) plotted as a function of time, spin-lattice relaxation time ( $T_1$ ) values were obtained (Figure 1g; see also the Experimental Section). It is known that the smaller  $T_1$  value indicates faster diffusion rate of the ions.<sup>[30,31]</sup> The SICSE showed a smaller  $T_1$  value (365 ms) than the C1 (1165 ms), demonstrating faster Li<sup>+</sup> mobility. In the SICSE, Li<sup>+</sup> ions rarely encounter anions because anions could be trapped by the ion-rectifying compliant skeleton, which can eventually boost Li<sup>+</sup> movement.

To develop high-energy-density SSLMBs, Li metal anodes should be coupled with high-voltage/high-capacity cathodes. This cell design draws attention to the electrochemical stability window of solid-state electrolytes.<sup>[32,33]</sup> For the SICSE, two anions (FSI<sup>−</sup> ions from the LiFSI salts and TFSI<sup>−</sup> ions from DADMA-TFSI of the cationic copolymers) exist in the double layers at the electrode–electrolyte interfaces. The anions in the double layers push solvent molecules away from the electrode surface,<sup>[34,35]</sup> beneficially contributing to the electrochemical stability of the SICSE. Driven by this anion-driven shielding effect, the SICSE showed a wider electrochemical stability window ( $\approx 5.7$  V (vs Li/Li<sup>+</sup>)) (Figure S14, Supporting Information), revealing its potential use in high-voltage full cells. The superior electrochemical stability of the SICSE was further verified by conducting an electrochemical floating test,<sup>[36]</sup> in which SSLMB cells (Li metal anode||NCM811 cathode in the presence of SICSE (vs C1)) were charged to 4.6 V under a low current rate of C/15 and then held at 4.65 and 4.7 V for 10 h while the current was being monitored. The leakage current of the cell

with the SICSE was lower than that of the control cell with the C1 over a whole range of charge voltages examined herein (Figure S15, Supporting Information). This result indicates that the electrochemical oxidation of the SICSE could be mitigated along with preventing the passivation of NCM811 cathode surface, confirming the anion-driven shielding effect of the SICSE.

## 2.2. Interfacial Stability of the SICSE with Li Metal Anode at Ambient Conditions

Critical current density (CCD), which is defined as a current density at which a cell is short-circuited, is a useful indicator for the interfacial stability of Li metal anode with electrolytes and dendrite growth.<sup>[37,38]</sup> Figure 2a shows Li plating/stripping profiles of the SICSE and C1 as a function of current density, in which the applied current density was increased from 0.1 to 2.0 mA cm<sup>−2</sup> with a step increase of 0.1 mA cm<sup>−2</sup> h<sup>−1</sup> (0.5 h stripping and 0.5 h plating). The SICSE showed a higher CCD (2.0 mA cm<sup>−2</sup>) than the C1 (CCD = 1.0 mA cm<sup>−2</sup>). This result was underscored by conducting a comparison with the CCD values of previously reported solid-state electrolytes that were characterized under high pressing conditions (Table S3, Supporting Information). Moreover, the SICSE, owing to its high ionic conductivity and single-ion conducting capability ( $t_{\text{Li}^+} = 0.91$ ), exhibited the lower overpotential than the C1 and moreover, maintained the rectangular shapes over a wide range of current densities. Notably, the “arc,” which is known to reflect the accumulation of dead Li,<sup>[39]</sup> was hardly observed at the SICSE compared to the C1, exhibiting its superior interfacial stability with Li metal anodes (Figure S16, Supporting Information). To confirm the superiority of the SICSE, a short-circuit time ( $T_{\text{sc}}$ ), which is related to the Sand's time,<sup>[40,41]</sup> was examined (Figure 2b). The SICSE allowed continuous charging for almost 200 h, whereas the C1 failed to charge after 63 h. This result demonstrated that the single-ion conducting capability ( $t_{\text{Li}^+} = 0.91$ ) of the SICSE played a crucial role in enabling stable Li plating on the Li metal anode surface, suppressing Li dendrite growth.

The Li plating/stripping behavior of the Li||Li symmetric cells was investigated. The cell containing the SICSE showed better Li plating/stripping cyclability when compared to the control (C1, C2, and C3) samples (Figure 2c). Furthermore, even at a higher current density of 1.0 mA cm<sup>−2</sup>, the SICSE still exhibited the stable Li plating/stripping cycling behavior (Figure S17, Supporting Information). The advantageous effect of the SICSE was confirmed by analyzing physicochemical and structural change of Li metal anodes, with focus on the comparison between the SICSE and C1. We investigated the cell impedance after the cycle test (Figure 2d). The SICSE showed a lower solid electrolyte interphase (SEI) resistance and charge transfer resistance than the C1, indicating the facile transport of Li<sup>+</sup> ions toward the Li metal anode owing to its single-ion conduction characteristic. To provide additional evidence, we examined structural change of the Li metal after the repeated Li plating/stripping test (80 cycles). For the C1, a number of needle-like Li dendrites and physically isolated Li particles were observed on the Li metal anode (inset of Figure 2e). In contrast, the SICSE allowed the Li metal anode to form a nodular, dense/uniform surface morphology (Figure 2e), due to the

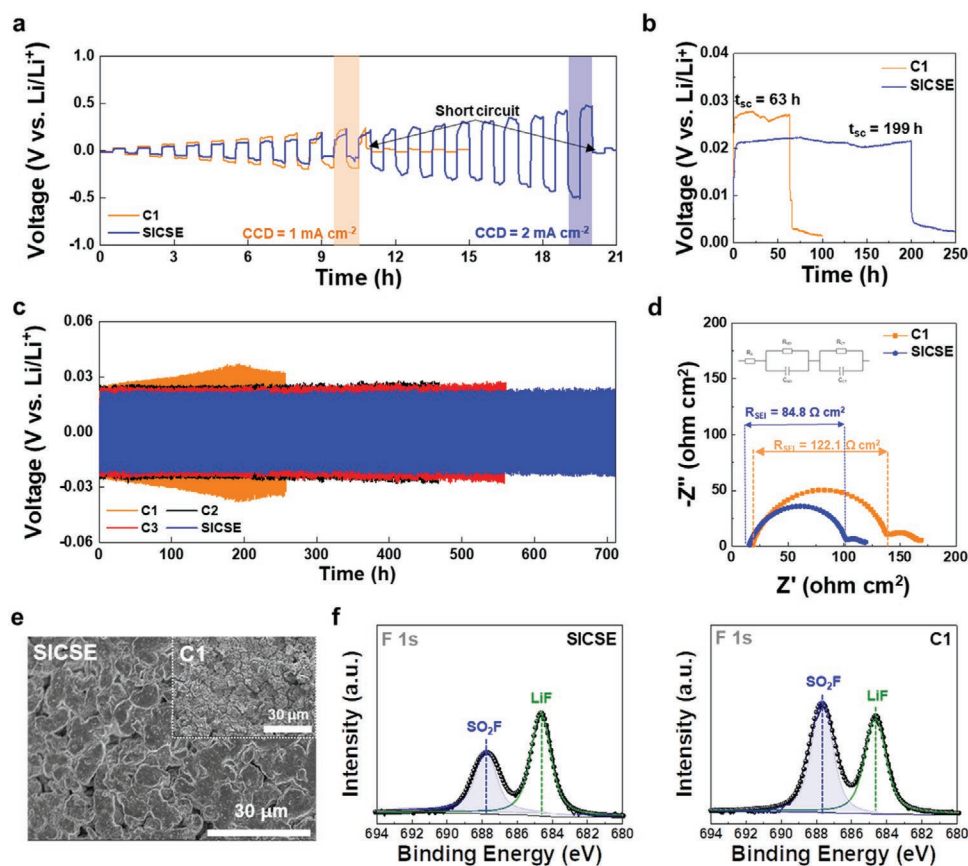


**Figure 2.** Interfacial stability of the SICSE with Li metal anode at ambient conditions. a) Li plating/stripping profiles of the SICSE and C1 as a function of current density, in which the applied current density was increased from 0.1 to 2.0 mA cm<sup>-2</sup> with a step increase of 0.1 mA cm<sup>-2</sup> h<sup>-1</sup> (0.5 h stripping and 0.5 h plating). b) Voltage profiles of the SICSE and C1 showing short-circuit time ( $t_{sc}$ ) at a fixed current density of 0.1 mA cm<sup>-2</sup>. c) Voltage profiles of Li||Li symmetric cells (SICSE vs control samples [C1, C2, and C3]) at current density of 0.1 mA cm<sup>-2</sup> and capacity of 0.1 mAh cm<sup>-2</sup>. d) EIS spectra of Li||Li symmetric cells with the SICSE and C1. e) SEM image (surface view) of the cycled Li metal anode (SICSE vs C1 (inset)). f) XPS F1s spectra of the cycled Li metal surfaces anode (SICSE vs C1).

suppression of unwanted interfacial side reactions between Li metal anodes and electrolytes. The X-ray photoelectron spectroscopy (XPS) analysis showed that the cycled Li metal (assembled with the SICSE) presented weaker intensities of characteristic peaks assigned to SO<sub>2</sub>F (at 687.7 eV)<sup>[42,43]</sup> which is known as a byproduct stemming from interfacial side reactions of anions with Li metal anodes (Figure 2f). In addition, the peak intensity ratio of LiF (at 684.6 eV, known as a SEI component that can mitigate Li dendrite growth<sup>[42,44]</sup>) to SO<sub>2</sub>F was larger at the SICSE compared to the result of the C1. This result exhibits that the SICSE, owing to the formation of LiF-rich SEI layer, can suppress the interfacial side reactions with Li metal anodes. This result demonstrated that the SICSE, as a well-designed single-ion conductor, can address the longstanding challenge of (anion-triggered) interfacial instability between conventional dual-ion conducting electrolytes and Li metal anode.

### 2.3. Electrochemical Performance of SSLMBs at Ambient Conditions

We explored potential applications of the SICSE to SSLMBs at ambient operating conditions, with a focus on its single-

ion conduction characteristic. To fabricate a SSLMB full cell, a NCM811 cathode (NCM811 particles/carbon conductive additives/gel electrolyte = 68/5/27 (w/w/w), without conventional cathode binders such as polyvinylidene fluoride (PVdF) and processing solvents such as NMP) was introduced on top of the SICSE-Li metal anode assembly through a UV-curing-assisted multistage printing process. The obtained SSLMB full cell was featured with the seamless integration of the Li metal anode, printed SICSE, and printed NCM811 cathode (Figure 3a). We note that the identical gel electrolyte (coordinate electrolyte/UV-cured cationic copolymer) existed in both the NCM811 cathode and SICSE (Figure S18, Supporting Information), thus acting as an ion-conducting interfacial glue. This unitized cell architecture is expected to play a key role in achieving reliable electrochemical performance and mechanical flexibility. The NCM811 cathode paste showed thixotropic fluid behavior which was similar to the rheological property of the SICSE, thereby enabling the fabrication of complex (e.g., letter)-shaped cathodes (Figure S19a,b, Supporting Information). The UV irradiation-driven polymerization of the monomer mixture in the NCM cathode was verified by monitoring the change in the FTIR peaks assigned to the acrylic C=C bonds (Figure S19c, Supporting Information).

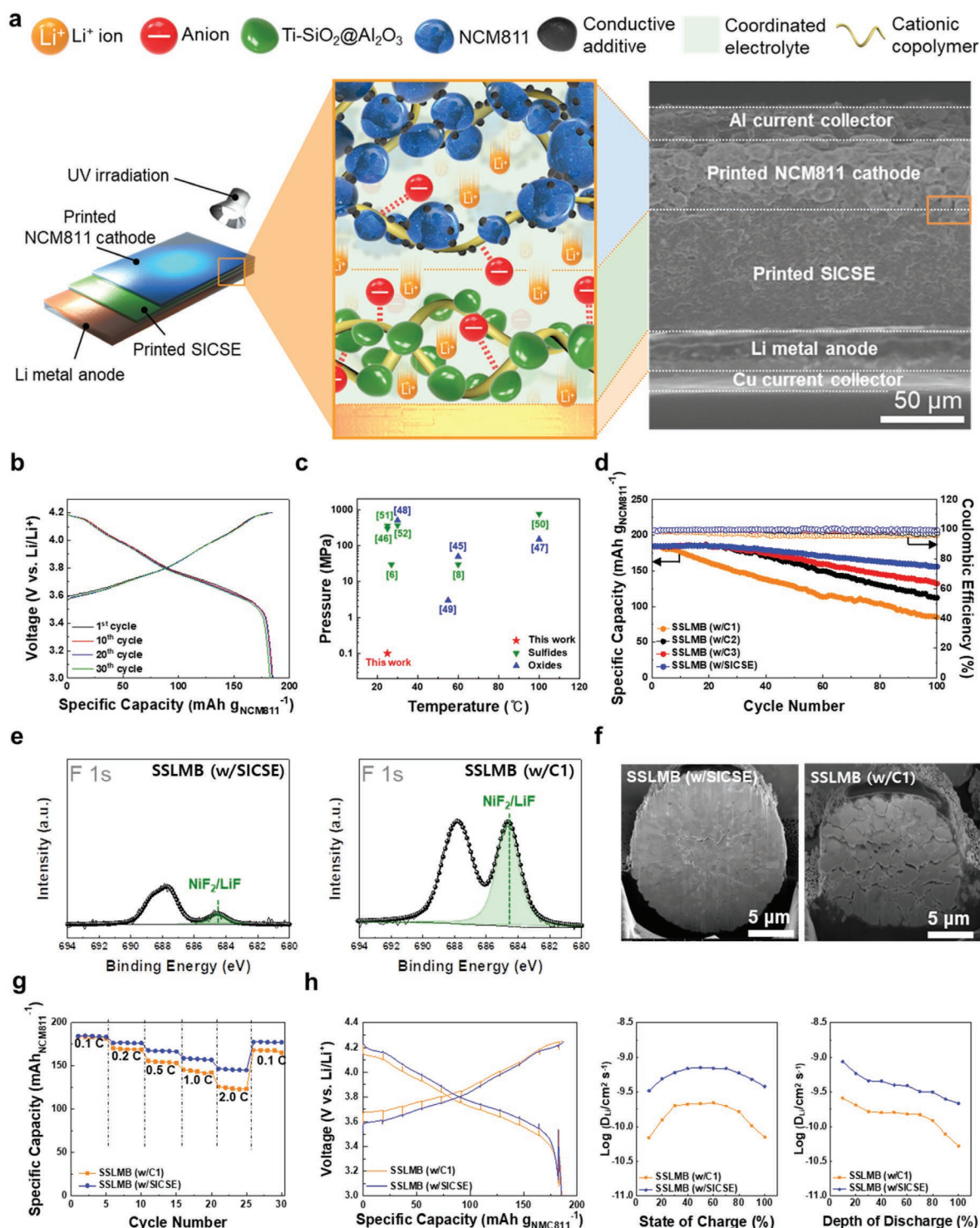


**Figure 3.** Electrochemical performance of the SSLMBs at ambient conditions. a) Conceptual illustration depicting the structure of the SSLMB fabricated through a UV-curing-assisted multistage printing process, along with its cross-sectional SEM image. b) Charge/discharge voltage profiles of the SSLMB as a function of cycle number under a voltage range of 3.0–4.2 V (vs Li/Li<sup>+</sup>) at a charge/discharge current density of 0.12/0.12 mA cm<sup>-2</sup>. c) Comparison of the cell operating conditions (pressure and temperature) between the SSLMBs and previously reported solid-state LMBs. d) Cycling performance of the SSLMBs (SICSE vs control samples [C1, C2, and C3]) at room temperature and ambient pressure. e) XPS F1s spectra of the cycled NCM811 particles (SSLMBs with SICSE vs SSLMBs with C1). f) FIB-SEM images of the cycled NCM811 particles (SSLMBs with SICSE vs SSLMBs with C1). g) Rate performance of the SSLMB with SICSE and SSLMB with C1, in which the discharge current density was varied from 0.1 to 2.0 C at a fixed charge current density of 0.1 C. h) GITT profiles (left) of the SSLMB with SICSE and SSLMB with C1 upon repeated current stimuli (at current density of 0.1 mA cm<sup>-2</sup> and interruption time between each pulse of 1 h) and Li<sup>+</sup> diffusion coefficients (right) as a function of SOC and DOD.



The SSLMB was cycled using a coin cell configuration under a voltage range of 3.0–4.2 V (vs Li/Li<sup>+</sup>) at a charge/discharge current density of 0.12/0.12 mA cm<sup>-2</sup>. The SSLMB exhibited normal and stable charge/discharge cycling performance, more notably, under ambient operating conditions (i.e., room temperature without external pressure) (Figure 3b). The ambient operation of the SSLMB is highly impressive, considering that most of the previously reported solid-state LMBs based on inorganic solid electrolytes<sup>[6,8,45–52]</sup> have shown cell performance under high-pressure/high-temperature conditions (Figure 3c).

The SSLMB with the SICSE exhibited higher cycling performance (capacity retention ≈ 84.5% after 100 cycles) compared to the SSLMBs with the control samples (C1, C2, and C3) (Figure 3d). This result was verified by conducting in-depth structural characterization, with particular focus on the comparison between the SICSE and C1. We examined the change in the EIS spectra during the cycling test. The growth of cell impedance after 100 cycles was not significant for the SSLMB with SICSE, as compared to the result of the SSLMB with C1 (Figure S20, Supporting Information). To better understand the superior cyclability of the SSLMB, we conducted a post-mortem analysis after the cycling test (100 cycles). The cycled Li metal of the SSLMB with SICSE exhibited the dense and uniform surface morphology compared to the result (a large number of randomly grown Li dendrites) at of the SSLMB with C1 (Figure S21, Supporting Information), which appeared consistent with the results of the Li/Li symmetric cells shown in Figure 2e. The cycled NCM811 particles of the SSLMB with SICSE showed the formation of a thin cathode electrolyte interphase (CEI) layer (≈7 nm), in comparison to those of the SSLMB with C1 showing a thick CEI layer (≈18 nm) (Figure S22, Supporting Information). The CEI layers were further analyzed using XPS and time-of-flight secondary ion mass spectroscopy (TOF-SIMS) analysis. A characteristic XPS F1s peak at 684.6 eV, corresponding to the LiF/NiF<sub>2</sub> byproducts formed by interfacial side reactions between electrolyte and cathode materials,<sup>[53]</sup> was substantially alleviated for the SSLMB with SICSE compared to those of the SSLMB with C1 (Figure 3e). This result was confirmed by TOF-SIMS analysis (Figure S23, Supporting Information). The formation of LiF/NiF<sub>2</sub> byproducts was suppressed with the SSLMB. In addition to the CEI layer characterization, the morphological change of the cycled NCM811 particles was examined using focused ion beam-scanning electron microscopy (FIB-SEM) and high-angle annular dark field-scanning transmission electron microscopy (HAADF-STEM). The cycled NCM811 particles of the SSLMB with SICSE maintained structural integrity whereas those of the SSLMB with C1 were severely cracked and disrupted (Figure 3f and Figure S24, Supporting Information). It is expected that the single-ion conducting capability of the SICSE in the SSLMB prevented the migration of anions that could trigger unwanted interfacial side reactions<sup>[54]</sup> with NCM811 particles, thereby contributing to the structural stabilization of the cycled NCM811 particles. This SICSE-driven beneficial effect on the NCM811 cathode, in combination with the stabilization of the Li metal anode (shown in Figure 2), enabled the improvement in the cycling performance of the SSLMB.

Figure 3g compares the discharge rate capability of the SSLMB with SICSE and the SSLMB with C1, in which the

discharge current density was varied from 0.1 to 2.0 C at a fixed charge current density of 0.1 C. The SSLMB with SICSE showed higher discharge capacities than the SSLMB with C1 over a wide range of discharge current densities. The faster rate performance of the SSLMB was verified by galvanostatic intermittent titration technique (GITT) analysis. Figure 3h shows that the SSLMB effectively suppressed the rise in cell polarization upon repeated current stimuli (at a current density of 0.1 C and interruption time between each pulse of 1 h). In addition, the SSLMB with SICSE showed higher Li<sup>+</sup> diffusion coefficients than the SSLMB with C1 over the entire range of the state of charge (SOC) and the depth of discharge (DOD). The detailed calculations on the ion diffusion coefficients<sup>[55]</sup> obtained from the GITT results are described in the experimental section. The facile redox kinetics of the SSLMB demonstrates the vital role of the single-ion conduction capability of the SICSE in mitigating the concentration polarization of the cell.

## 2.4. Beyond Traditional Solid-State LMBs

To develop a high-energy-density SSLMB full cell, the above-prepared NCM811 cathode (1.8 mAh cm<sup>-2</sup>) was coupled with a thin Li metal anode (≈20 μm) in the presence of SICSE (Figure S25, Supporting Information). In addition, the charge cut-off voltage was raised to 4.6 V under a 0.1 C/0.1 C charge/discharge rate. Under this harsh cut-off voltage, the obtained SSLMB showed decent charge/discharge cycling retention at ambient operating conditions (Figure 4a). The result of the SSLMB was compared with those of previously reported solid-state LMBs (Table S4, Supporting Information). The previous work has often used thick Li metal anodes and thick solid-state electrolytes to ensure electrochemical reliability of the solid-state LMB, resulting in the loss of volumetric cell energy densities.

Single-ion conductors can improve low-temperature cell performance owing to a suppression of concentration polarization at the electrodes.<sup>[56]</sup> The SSLMB with SICSE showed stable charge/discharge profiles over a wide range of temperatures (–10 to 10 °C) (Figure 4b), whereas the SSLMB with C1 failed to maintain electrochemical activity below –10 °C. Notably, the SSLMB successfully operated a light-emitting diode (LED) lamp under harsh temperature of –27.1 °C (Figure S26, Supporting Information). This excellent low-temperature cell performance was verified by analyzing the EIS profiles of the cells at –30 °C (Figure S27, Supporting Information). The SSLMB with SICSE exhibited a lower SEI resistance ( $R_{\text{SEI}}$ ) and charge transfer resistance ( $R_{\text{ct}}$ ) than the SSLMB with C1. Meanwhile, both the SICSE and C1 did not show any crystalline phases in differential scanning calorimetry (DSC) thermograms (Figure S28, Supporting Information), revealing that the low-temperature cell performance of the SSLMB is ascribed mainly to the single-ion conduction characteristic ( $t_{\text{Li}^+} = 0.91$ ) of the SICSE and the stabilized SICSE–electrode interfaces, not the differences in the bulk thermodynamic states between the SICSE and C1.

One of the formidable challenges facing solid-state LMBs based on inorganic solid electrolytes is the lack of mechanical flexibility. In sharp contrast, the SSLMB, due to the highly deformable printed SICSE, printed NCM811 cathode (Figure S29, Supporting Information), and monolithic integration of the cell

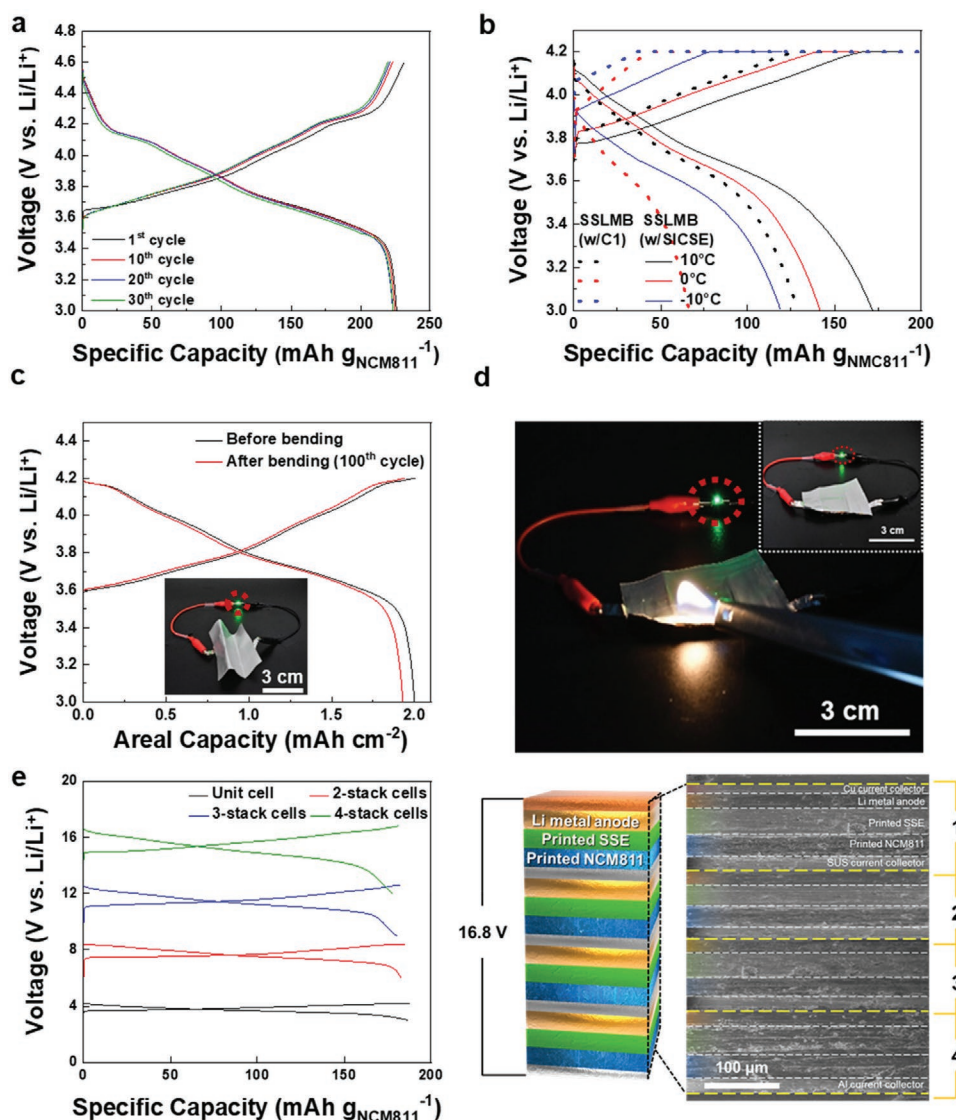


**Figure 4.** Beyond traditional solid-state LMB. a) High-voltage operation: charge/discharge voltage profiles of the 4.6 V-charged SSLMB with SICSE (Li ( $\approx 20 \mu\text{m}$ ) anode||NCM811 cathode) at a charge/discharge current density of  $0.18/0.18 \text{ mA cm}^{-2}$ . b) Low-temperature performance: charge/discharge voltage profiles of the SSLMBs as a function of operating temperature ( $-10$  to  $10^\circ\text{C}$ ). c) Mechanical flexibility: charge/discharge voltage profiles (expressed as areal capacities) of the SSLMB with SICSE before and after bending (bending radius =  $5 \text{ mm}$  and deformation rate =  $30 \text{ mm min}^{-1}$ ). Inset shows that the multiple-folded SSLMB powered an LED lamp. d) Nonflammability: safety tests of the SSLMB with SICSE. The SSLMB was cut in half horizontally and continued to power an LED lamp without explosion (inset) and even upon exposure to a flame. e) Bipolar configuration: charge/discharge voltage profiles (left) of the bipolar SSLMBs with SICSE (at a charge/discharge current density of  $0.1 \text{ C}/0.1\text{C}$ ) as a function of stacked cells. Cross-sectional SEM image (right) of the bipolar SSLMB with four cells stacked in series.

components enabled by the multistage printing, is expected to be physically flexible. To investigate mechanical flexibility of the SSLMB, a pouch-type cell (length  $\times$  width =  $18 \times 18 \text{ (mm mm}^{-1}\text{)}$ , capacity =  $2.0 \text{ mAh cm}^{-2}$ ) was fabricated. The obtained SSLMB, after the 100th bending cycle (bending radius =  $5 \text{ mm}$  and deformation rate =  $30 \text{ mm min}^{-1}$ ), showed no significant change in the charge/discharge profiles (Figure 4c and Figure S30, Supporting Information). Moreover, the SSLMB powered an LED lamp even after being folded multiple times (inset of Figure 4c and Movie S1, Supporting Information).

Despite the use of solid-state electrolytes in solid-state LMBs, there have been very few studies reporting the cell safety, to the

best of our knowledge. To address this issue, we examined the safety behavior of the SSLMB. The fully charged SSLMB was placed in a hot box (set to  $100^\circ\text{C}$ ) and its voltage change was traced as a function of elapsed time. The SSLMB maintained its voltage, whereas a control cell with conventional liquid electrolyte ( $1 \text{ M LiTFSI}$  in  $\text{EC/DMC} = 1/1 \text{ (v/v)}$ ) was severely swollen and dimensionally distorted (Figure S31, Supporting Information). After being horizontally cut in half, the SSLMB operated a LED lamp without explosion and structural disruption (Figure 4d and Movie S2, Supporting Information). Notably, the cut SSLMB continuously powered the LED lamp, even upon exposure to flame. Such exceptional safety of the SSLMB is



attributed to the nonflammable SICSE (Figure S32, Supporting Information) enabled by the coordinated electrolyte (4 M LiFSI in PC/FEC).<sup>[57]</sup> These results underscored the viability of the SICSE as a promising alternative to inorganic solid electrolytes.

We explored the potential feasibility of the SSLMB in bipolar cell configurations<sup>[21]</sup> that can provide higher cell voltages than a unit cell. On top of the SSLMB unit cell, UV-curing-assisted multistage printing was repeatedly performed to fabricate bipolar SSLMBs with an in-series configuration by sharing stainless steel (SUS) current collectors (Figure S33a, Supporting Information). The pouch-type bipolar SSLMB with SICSE showed normal and stable charge/discharge profiles (at a charge/discharge current density of 0.1 C/0.1 C) over the entire stacked cells examined herein (Figure 4e (left)). The full-charge voltages of the bipolar SSLMBs were linearly proportional to the number of serially stacked cells (Figure S33b, Supporting Information), exhibiting facile control of cell voltages through the bipolar cell configuration. More notably, a cell voltage of 16.656 V was achieved with the bipolar SSLMB (4 cells stacked in-series, Figure 4e (right)), which has never been reported in the previous studies of solid-state LMBs. Furthermore, the bipolar SSLMB with four-stacked cells showed the stable cycling performance along with high gravimetric/volumetric energy densities ( $476 \text{ Wh kg}_{\text{cell}}^{-1}/1102 \text{ Wh L}_{\text{cell}}^{-1}$ , Figure S34, Supporting Information), in which the gravimetric/volumetric energy densities of cells were estimated based on the weight/volume of cathodes, anodes, current collectors, and solid-state electrolytes (see Table S5, Supporting Information, for calculation details). These results demonstrated that the bipolar SSLMBs can be used as a practical power source with tunable operating voltages and high energy densities.

A comparison (Table S4b, Supporting Information) with previously reported solid-state LMBs showed that the SSLMB enabled improvements in the mechanical flexibility, nonflammability, and the number of bipolar-stacked cells in addition to the electrochemical superiority (including the operating conditions, cyclability, rate capability, and low-temperature performance) described above, underscoring the validity of SICSE as a promising solid-state electrolyte candidate for practical solid-state LMBs.

### 3. Conclusion

In summary, we have demonstrated the SICSE as a new quasi-solid-state electrolyte strategy for practical SSLMBs that enable cell fabrication and operation under ambient conditions. The SICSE was composed of the nonflammable coordinated electrolyte and ion-rectifying compliant skeleton (cationic copolymer/Ti-SiO<sub>2</sub>@Al<sub>2</sub>O<sub>3</sub>). Combining the thixotropic SICSE paste with the UV-curing-assisted multistage printing process allowed the fabrication of the seamlessly integrated SSLMB without requiring high-temperature/high-pressure sintering steps. The soft feature of the SICSE addressed the concerns on grain-boundary resistance and the interfacial instability of the electrolytes-electrodes, which have posed longstanding challenges in inorganic solid electrolytes. The single-ion conducting capability of the SICSE allowed the formation of stable interfaces with the Li metal anodes and NCM811 cathodes.

Driven by the SICSE and the monolithic cell architecture, the SSLMB exhibited stable charge/discharge performance (cycling retention, rate capability, and bipolar configurations with tunable voltages and high gravimetric/volumetric energy densities ( $476 \text{ Wh kg}_{\text{cell}}^{-1}/1102 \text{ Wh L}_{\text{cell}}^{-1}$  at four-stacked cells with 16.656 V) under ambient operating conditions. Moreover, the low-temperature performance, mechanical flexibility, and safety (nonflammability) were achieved for the SSLMB, which far exceeded those of the previously reported solid-state LMBs. The SICSE described herein can be suggested as a promising single-ion conducting solid-state electrolyte platform that can lead us closer to the practically viable solid-state LMBs.

### 4. Experimental Section

**Synthesis of SICSEs and Fabrication of SSLMBs at Ambient Conditions:** To synthesize the SICSE, PC (anhydrous,  $\geq 99.7\%$ ), FEC (anhydrous,  $\geq 99\%$ ), ETPTA, and HMPP were purchased from Sigma-Aldrich. LiFSI ( $\geq 99.9\%$ , LG Chem) was used as-received. The coordinate electrolyte was prepared by mixing the corresponding solvents and lithium salts in crimp-cap sealed vials. DADMA-TFSI (Figure S35, Supporting Information) and silica-oxygen-titanium (Si-O-Ti)-coated alumina (Al<sub>2</sub>O<sub>3</sub>) nanoparticles (Ti-SiO<sub>2</sub>@Al<sub>2</sub>O<sub>3</sub>) (Figure S36, Supporting Information) were prepared using the synthetic procedures of previous reports,<sup>[25,58]</sup> respectively. The morphology of Ti-SiO<sub>2</sub>@Al<sub>2</sub>O<sub>3</sub> was characterized using field emission transmission electron microscopy (FETEM, JEM-2100F, JEOL). The chemical structure of the cationic copolymer was characterized using an Agilent VNMRS 600 MHz solid-state NMR spectrometer at room temperature. The direct polarization magic angle spinning (DP-MAS) <sup>1</sup>H NMR spectra were recorded under 20 kHz spinning rate and referenced to hexamethylbenzene at 2.2 ppm as an external standard. The molecular weight information of the cationic copolymer was obtained using GPC (Agilent 1200S/miniDAWN TREOS, Agilent/Wyatt). For this GPC analysis, the cationic copolymer was dissolved in tetrahydrofuran (THF) solvent, and polyethylene was chosen as a reference for the calibration of molecular weight. An optimal composition ratio (coordinated electrolyte (4 M LiFSI in PC/FEC = 93/7 (v/v)/compliant skeleton precursor) of the SICSE paste was set as 42.5/57.5 (w/w), in which a composition ratio of the compliant skeleton precursor was UV-curable monomer mixture/Ti-SiO<sub>2</sub>@Al<sub>2</sub>O<sub>3</sub> nanoparticles ( $\approx 500 \text{ nm}$ ) = 50/50 (w/w) and a composition ratio of the UV-curable monomer mixture was ETPTA/DADMA-TFSI = 40/60 (w/w). The SICSE paste (i.e., prior to UV curing) was stencil-printed directly on a Li metal foil (Honjo Metal Co., Ltd., thickness = 20  $\mu\text{m}$ ) without using any processing solvents and then cured after exposure to UV irradiation for less than 30 s. The UV irradiation was performed using an Hg UV-lamp (Lichtzen) with an irradiation peak intensity of  $\approx 2000 \text{ mW cm}^{-2}$ . Subsequently, the LiNi<sub>0.8</sub>Co<sub>0.1</sub>Mn<sub>0.1</sub>O<sub>2</sub> (NCM811) cathode was fabricated by printing the NCM811 cathode paste (NCM811 active materials/carbon conductive additives/gel electrolyte precursor (coordinated electrolyte/UV-curable monomer mixture = 85/15 (w/w) = 68/5/27 (w/w/w)) directly onto the SICSE layer/Li metal anode assembly, followed by UV irradiation. The NCM811 active materials and carbon conductive additives were provided from LG Energy Solution. After the aluminum (Al) current collector was placed on top of the printed NCM811 cathode/printed SICSE layer/Li metal anode assembly, a seamlessly integrated SSLMB full cell was obtained. The areal mass loading of NCM811 materials in the printed NCM811 cathode was  $9 \text{ mg cm}^{-2}$ . A pouch-type cell SSLMBs unit cell (length  $\times$  width =  $18 \times 18 \text{ (mm/mm)}$ ), capacity =  $2.0 \text{ mAh cm}^{-2}$ ) was fabricated. On top of the as-prepared SSLMBs unit cell, the UV curing-assisted printing process was repeatedly conducted, eventually fabricating the bipolar SSLMBs (with in-series configuration). To enable this bipolar cell configuration, the NCM811 cathode and Li metal anode shared a stainless steel foil (SUS) as a common current collector. The bipolar cells were sealed with an Al pouch as a packaging

substance. The whole fabrication process of the cells was carried out in a dry room at room temperature and ambient pressure.

**Physicochemical/Electrochemical Characterization of SICSEs:** The UV-curing reaction of the SICSE was examined using a FTIR spectrometer (Alpha Platinum ATR, Bruker) with a spectral resolution of 4 cm<sup>-1</sup>. The weight loss of the SICSE was estimated as a function of temperature using a thermogravimetric analyzer (Q500, TA Instruments, heating rate = 10 °C min<sup>-1</sup>) under a nitrogen atmosphere. The rheological properties of the NCM811 cathode paste and SICSE paste were investigated using a rheometer (Haake MARS 3, Thermo Electron GmbH). The morphologies of the SICSEs and their components were characterized using field-emission scanning electron microscopy (S-4800, Hitachi) equipped with EDS and thermogravimetric analysis (TGA). The Li<sup>+</sup> transference number ( $t_{Li^+}$ ) was evaluated using a potentiostatic polarization method. The DC polarization through a Li<sup>+</sup> non-blocking symmetric cell and its sequential EIS before/after the polarization was analyzed to determine the Li<sup>+</sup> transference number<sup>[22]</sup>

$$t_{Li^+} = \frac{I_s(\Delta V - I_0 R_0)}{I_0(\Delta V - I_s R_s)} \quad (1)$$

where  $\Delta V$  is applied potential,  $I_0$  and  $R_0$  are the initial current and resistance, and  $I_s$  and  $R_s$  are the steady-state current and resistance after the polarization, respectively. The surface characteristics of the Ti-SiO<sub>2</sub>@Al<sub>2</sub>O<sub>3</sub> nanoparticles were investigated by conducting XPS (ESCALAB 250XI, Thermo Fisher), inductively coupled plasma optical emission spectrometry (ICP-OES, Varian 700-ES), and zeta potential measurement (Zetasizer Nano ZS, Malvern Instruments Inc.). The in situ FTIR spectroscopy was used to test and characterize the surface composition of Ti-SiO<sub>2</sub>@Al<sub>2</sub>O<sub>3</sub> nanoparticles. The electrostatic interaction between positively charged SICSE and free anions were traced by using a FTIR (Alpha Platinum ATR, Bruker). The DSC measurement was carried out in a DSC Q200 (TA Instruments). During the measurement, the sealed pan with electrolyte was firstly cooled down to -70 °C at a scan rate of 5 °C min<sup>-1</sup> using liquid nitrogen cooling system, then equilibrated at -70 °C, finally followed with a test procedure scanning from -70 to 120 °C at a scan rate of 5 °C min<sup>-1</sup>. The ion conductivity was measured with an Li<sup>+</sup> blocking symmetric cell based on an EIS analysis at a frequency range from 10<sup>-2</sup> to 10<sup>6</sup> Hz and an applied amplitude of 10 mV. The impedance was measured from -20 to 100 °C. The ionic conductivity ( $\sigma$ ) was determined according to following equation

$$\sigma = \frac{L}{RA} \quad (2)$$

where  $L$  is the pellet thickness,  $R$  is the resistance, and  $A$  is the area in contact with the electrodes. The activation energy ( $E_a$ ) for ion conduction was determined from the slope of the Arrhenius plot. Solid-state NMR experiments were carried out using an Agilent VNMRs 600 MHz FT-NMR spectrometer equipped with 1.6 mm HXY fastMAS probe and spinning at 20 kHz. All experiments were acquired at room temperature. <sup>7</sup>Li chemical shifts were referenced to a 1.0 M aqueous LiCl solution at 0.0 ppm as an external standard. Parameters were 20.0 s for recycle delay time and 1.5 μs for <sup>7</sup>Li 90° pulse length. Spin-lattice relaxation time ( $T_1$ ) was measured using an inversion saturation recovery pulse sequence with 16 saturation pulses at interpulse delay varying from 0.5 to 32.0 s. The spectra were acquired at 20.0 kHz MAS rate in a 1.6 mm zirconium rotor and the isotropic resonances were integrated to obtain  $T_1$  according to following equation<sup>[30,31]</sup>

$$I = I_0(1 - \exp^{-t/T_1}) \quad (3)$$

where  $I$  is the peak intensity at time  $t$ ,  $I_0$  is the saturation intensity, and  $T_1$  is the longitudinal relaxation constant. The Li plating/stripping cyclability of symmetric Li (100 μm)||Li (100 μm) cells was conducted at a current density of 1 mA cm<sup>-2</sup> with an areal capacity of 1 mAh cm<sup>-2</sup>. The EIS of the Li||Li cells was recorded using a potentiostat (VSP classic, Bio-Logic) over the frequency range 10<sup>-2</sup>–10<sup>6</sup> Hz. The electrochemical stability windows of the electrolytes were evaluated via linear sweep

voltammetry (LSV) at a scan rate of 0.1 mV s<sup>-1</sup> using an asymmetric cell (SUS||Li) at room temperature. The Li<sup>+</sup> diffusion coefficients in the SSLMB electrodes were obtained using GITT. This GITT analysis was conducted under the following measurement condition: a galvanostatic pulse of 1 h at a current density of 0.1 C followed by a 1 h interruption time between the pulses (Figure 3h). We calculated the Li<sup>+</sup> diffusion coefficients using the following equation<sup>[55]</sup>

$$D = \frac{4}{\pi \tau} \left( \frac{V_m n_m}{S} \right)^2 \left( \frac{\Delta E_s}{\Delta E_t} \right)^2 \quad (4)$$

wherein  $t$  and  $\tau$  represent the duration of current pulse (s) and relaxation time (s), respectively;  $n_m$  and  $V_m$  are the moles of NCM811 and molar volume;  $S$  is the electrode-electrolyte interface area (taken as the geometric area of the electrode);  $\Delta E_s$  and  $\Delta E_t$  are the steady-state voltage change (V) by the current pulse and overall cell voltage change (V) during the constant current pulse in a single step GITT measurement, respectively.

**Electrochemical Performance, Flexibility, and Safety of SSLMBs:** The charge/discharge performance of the SSLMBs was investigated with CR2032-type coin and pouch-type cells using a cycle tester (PNE Solution Co., Ltd, Korea). The post-mortem analysis after the charge/discharge cycling test was conducted using XPS (ESCALAB 250XI, Thermo Fisher) with monochromatized Al K $\alpha$  radiation. The electrodes were removed from the cells after 100 cycles and rinsed with DMC inside a glove box. All samples were vacuum-dried overnight and then transferred into a XPS chamber. The working pressure of the chamber was lower than 6.6 × 10<sup>-9</sup> Pa. All reported binding energy values were calibrated to the C 1s peak at 284.8 eV. After cycling test, the morphology of the Li metal anode surface was analyzed using FESEM (S-4800, HITACHI). The morphology of the CEI layers in the NCM811 cathodes was characterized by high-resolution transmission electron microscopy (HRTEM) (JEM-2100F, JEOL). The time-of-flight secondary ion mass spectroscopy (ToF-SIMS) was performed using a TOF-SIMS 5 (ION TOF) with a Bi<sub>3</sub><sup>2+</sup> gun at 50 keV to analyze byproducts of the NCM811 cathode. A FIB (Helios Nano Lab450, FEI) was used to analyze the cross-sectional structure of the NCM811 particles. The HAADF-STEM images were taken using a probe-side aberration corrected TEM. The mechanical flexibility of the SSLMBs was investigated under various deformation modes such as bending, winding, and multiple folding. The safety of the SSLMB was examined under various harsh conditions (including horizontal cutting and exposure to flame).

## Supporting Information

Supporting Information is available from the Wiley Online Library or from the author.

## Acknowledgements

This work was supported by the Basic Science Research Program (2016R1A5A1009926, 2017M1A2A2087812, 2018M3D1A1058744, and 2021R1A2B5B03001615) through the National Research Foundation of Korea (NRF) grant by the Korean Government (MSIT) and Yonsei University Research Fund of 2020-22-0536.

## Conflict of Interest

The authors declare no conflict of interest.

## Data Availability Statement

Research data are not shared.

## Keywords

ambient operation, lithium metal batteries, multistage printing, single-ion conductors, soft electrolytes

Received: June 12, 2021

Revised: July 23, 2021

Published online: August 8, 2021

- [1] R. Schmich, R. Wagner, G. Höpfer, T. Placke, M. Winter, *Nat. Energy* **2018**, 3, 267.
- [2] M. Winter, B. Barnett, K. Xu, *Chem. Rev.* **2018**, 118, 11433.
- [3] J. Janek, W. G. Zeier, *Nat. Energy* **2016**, 1, 16141.
- [4] A. Manthiram, X. Yu, S. Wang, *Nat. Rev. Mater.* **2017**, 2, 16103.
- [5] A. Banerjee, X. Wang, C. Fang, E. A. Wu, Y. S. Meng, *Chem. Rev.* **2020**, 120, 6878.
- [6] N. Kamaya, K. Homma, Y. Yamakawa, M. Hirayama, R. Kanno, M. Yonemura, T. Kamiyama, Y. Kato, S. Hama, K. Kawamoto, A. Mitsui, *Nat. Mater.* **2011**, 10, 682.
- [7] X. Miao, H. Wang, R. Sun, C. Wang, Z. Zhang, Z. Li, L. Yin, *Energy Environ. Sci.* **2020**, 13, 3780.
- [8] Y.-G. Lee, S. Fujiki, C. Jung, N. Suzuki, N. Yashiro, R. Omoda, D.-S. Ko, T. Shiratsuchi, T. Sugimoto, S. Ryu, J. H. Ku, T. Watanabe, Y. Park, Y. Aihara, D. Im, I. T. Han, *Nat. Energy* **2020**, 5, 299.
- [9] M. B. Armand, *Annu. Rev. Mater. Sci.* **1986**, 16, 245.
- [10] T. Dong, J. Zhang, G. Xu, J. Chai, H. Du, L. Wang, H. Wen, X. Zang, A. Du, Q. Jia, X. Zhou, G. Cui, *Energy Environ. Sci.* **2018**, 11, 1197.
- [11] D. Zhou, D. Shanmukaraj, A. Tkacheva, M. Armand, G. Wang, *Chem* **2019**, 5, 2326.
- [12] Q. Zhao, S. Stalin, C.-Z. Zhao, L. A. Archer, *Nat. Rev. Mater.* **2020**, 5, 229.
- [13] S. Xia, X. Wu, Z. Zhang, Y. Cui, W. Liu, *Chem* **2019**, 5, 753.
- [14] K. Jeong, S. Park, S.-Y. Lee, *J. Mater. Chem. A* **2019**, 7, 1917.
- [15] Y. Tian, T. Shi, W. D. Richards, J. Li, J. C. Kim, S.-H. Bo, G. Ceder, *Energy Environ. Sci.* **2017**, 10, 1150.
- [16] Y. Lu, L. Li, Q. Zhang, Z. Niu, J. Chen, *Joule* **2018**, 2, 1747.
- [17] Z. Ding, J. Li, J. Li, C. An, *J. Electrochem. Soc.* **2020**, 167, 070541.
- [18] S. Chen, J. Zhang, L. Nie, X. Hu, Y. Huang, Y. Yu, W. Liu, *Adv. Mater.* **2021**, 33, 2002325.
- [19] K. Xu, *Chem. Rev.* **2014**, 114, 11503.
- [20] K. H. Choi, J. T. Yoo, C. K. Lee, S. Y. Lee, *Energy Environ. Sci.* **2016**, 9, 2812.
- [21] S. H. Kim, K. H. Choi, S. J. Cho, J. Yoo, S. S. Lee, S. Y. Lee, *Energy Environ. Sci.* **2018**, 11, 321.
- [22] J. Evans, C. A. Vincent, P. G. Bruce, *Polymer* **1987**, 28, 2324.
- [23] G. Li, Z. Liu, Q. Huang, Y. Gao, M. Regula, D. Wang, L.-Q. Chen, D. Wang, *Nat. Energy* **2018**, 3, 1076.
- [24] G. Li, Z. Liu, D. Wang, X. He, S. Liu, Y. Gao, A. AlZahrani, S. H. Kim, L. Q. Chen, D. Wang, *Adv. Energy Mater.* **2019**, 9, 1900704.
- [25] S. K. Cho, H. I. Kim, J. W. An, K. Jung, H. Bae, J. H. Kim, T. Yim, S. Y. Lee, *Adv. Funct. Mater.* **2020**, 30, 2070157.
- [26] R. Garro, M. T. Navarro, J. Primo, A. Corma, *J. Catal.* **2005**, 233, 342.
- [27] H. Song, J. Wang, Z. Wang, H. Song, F. Li, Z. Jin, *J. Catal.* **2014**, 311, 257.
- [28] P. C. Stair, *J. Am. Chem. Soc.* **1982**, 104, 4044.
- [29] D. A. Vazquez-Molina, G. S. Mohammad-Pour, C. Lee, M. W. Logan, X. Duan, J. K. Harper, F. J. Uribe-Romo, *J. Am. Chem. Soc.* **2016**, 138, 9767.
- [30] H. Chen, H. Tu, C. Hu, Y. Liu, D. Dong, Y. Sun, Y. Dai, S. Wang, H. Qian, Z. Lin, L. Chen, *J. Am. Chem. Soc.* **2018**, 140, 896.
- [31] N. Wu, P. H. Chien, Y. Qian, Y. Li, H. Xu, N. S. Grundish, B. Xu, H. Jin, Y. Y. Hu, G. Yu, J. B. Goodenough, *Angew. Chem., Int. Ed.* **2020**, 59, 4131.
- [32] Z. Li, H. Zhang, X. Sun, Y. Yang, *ACS Energy Lett.* **2020**, 5, 3244.
- [33] H. Yuan, J. Luan, Z. Yang, J. Zhang, Y. Wu, Z. Lu, H. Liu, *ACS Appl. Mater. Interfaces* **2020**, 12, 7249.
- [34] S. Jiao, X. Ren, R. Cao, M. H. Engelhard, Y. Liu, D. Hu, D. Mei, J. Zheng, W. Zhao, Q. Li, N. Liu, B. D. Adams, C. Ma, J. Liu, J.-G. Zhang, W. Xu, *Nat. Energy* **2018**, 3, 739.
- [35] J. Alvarado, M. A. Schroeder, T. P. Pollard, X. Wang, J. Z. Lee, M. Zhang, T. Wynn, M. Ding, O. Borodin, Y. S. Meng, K. Xu, *Energy Environ. Sci.* **2019**, 12, 780.
- [36] Y. Li, G. M. Veith, K. L. Browning, J. Chen, D. K. Hensley, M. P. Paranthaman, S. Dai, X.-G. Sun, *Nano Energy* **2017**, 40, 9.
- [37] H. Huo, Y. Chen, R. Li, N. Zhao, J. Luo, J. G. Pereira Da Silva, R. Mücke, P. Kaghazchi, X. Guo, X. Sun, *Energy Environ. Sci.* **2020**, 13, 127.
- [38] K. B. Hatzell, X. C. Chen, C. L. Cobb, N. P. Dasgupta, M. B. Dixit, L. E. Marbella, M. T. McDowell, P. P. Mukherjee, A. Verma, V. Viswanathan, A. S. Westover, W. G. Zeier, *ACS Energy Lett.* **2020**, 5, 922.
- [39] K.-H. Chen, K. N. Wood, E. Kazyak, W. S. LePage, A. L. Davis, A. J. Sanchez, N. P. Dasgupta, *J. Mater. Chem. A* **2017**, 5, 11671.
- [40] P. Bai, J. Li, F. R. Brushett, M. Z. Bazant, *Energy Environ. Sci.* **2016**, 9, 3221.
- [41] Y. Lu, M. Tikekar, R. Mohanty, K. Hendrickson, L. Ma, L. A. Archer, *Adv. Energy Mater.* **2015**, 5, 1402073.
- [42] X. Fan, L. Chen, X. Ji, T. Deng, S. Hou, J. Chen, J. Zheng, F. Wang, J. Jiang, K. Xu, C. Wang, *Chem* **2018**, 4, 174.
- [43] L. Suo, W. Xue, M. Gobet, S. G. Greenbaum, C. Wang, Y. Chen, W. Yang, Y. Li, J. Li, *Proc. Natl. Acad. Sci. USA* **2018**, 115, 1156.
- [44] X. Fan, X. Ji, F. Han, J. Yue, J. Chen, L. Chen, T. Deng, J. Jiang, C. Wang, *Sci. Adv.* **2018**, 4, eaau9245.
- [45] Z. Yang, H. Yuan, C. Zhou, Y. Wu, W. Tang, S. Sang, H. Liu, *Chem. Eng. J.* **2020**, 392, 123650.
- [46] F. Zhao, J. Liang, C. Yu, Q. Sun, X. Li, K. Adair, C. Wang, Y. Zhao, S. Zhang, W. Li, S. Deng, R. Li, Y. Huang, H. Huang, L. Zhang, S. Zhao, S. Lu, X. Sun, *Adv. Energy Mater.* **2020**, 10, 1903422.
- [47] M. Finsterbusch, T. Danner, C.-L. Tsai, S. Uhlenbruck, A. Latz, O. Guillon, *ACS Appl. Mater. Interfaces* **2018**, 10, 22329.
- [48] S. Yu, A. Mertens, H. Tempel, R. Schierholz, H. Kungl, R.-A. Eichel, *ACS Appl. Mater. Interfaces* **2018**, 10, 22264.
- [49] K. Arbi, J. M. Rojo, J. Sanz, *J. Eur. Ceram. Soc.* **2007**, 27, 4215.
- [50] D. H. Kim, D. Y. Oh, K. H. Park, Y. E. Choi, Y. J. Nam, H. A. Lee, S.-M. Lee, Y. S. Jung, *Nano Lett.* **2017**, 17, 3013.
- [51] R. Xu, J. Yue, S. Liu, J. Tu, F. Han, P. Liu, C. Wang, *ACS Energy Lett.* **2019**, 4, 1073.
- [52] D. Y. Oh, Y. J. Nam, K. H. Park, S. H. Jung, K. T. Kim, A. R. Ha, Y. S. Jung, *Adv. Energy Mater.* **2019**, 9, 1802927.
- [53] S. Jiao, J. Zheng, Q. Li, M. H. Engelhard, R. Cao, J.-G. Zhang, W. Xu, *Joule* **2018**, 2, 110.
- [54] H. Q. Pham, J. Lee, H. M. Jung, S. W. Song, *Electrochim. Acta* **2019**, 317, 711.
- [55] C. Hong, Q. Leng, J. Zhu, S. Zheng, H. He, Y. Li, R. Liu, J. Wan, Y. Yang, *J. Mater. Chem. A* **2020**, 8, 8540.
- [56] Z. Lin, J. Liu, *RSC Adv.* **2019**, 9, 34601.
- [57] S. J. Cho, D. E. Yu, T. P. Pollard, H. Moon, M. Jang, O. Borodin, S. Y. Lee, *iScience* **2020**, 23, 100844.
- [58] Z. Qiu, S. Yuan, Z. Wang, L. Shi, J. H. Jo, S. T. Myung, J. Zhu, *J. Power Sources* **2020**, 472, 228445.